ELSEVIER

Polymer 42 (2001) 5651–5659

polymer

www.elsevier.nl/locate/polymer

Morphology evolution of immiscible polymer blends in complex flow fields

Concetta Testa, Immacolata Sigillo, Nino Grizzuti*

Department of Chemical Engineering, University of Naples Federico II, Piazzale V. Tecchio, 80-80125 Napoli, Italy

Received 19 July 2000; received in revised form 23 January 2001; accepted 24 January 2001

Abstract

A transparent flow cell apparatus has been used to obtain quantitative information on the morphology evolution of a model polymer blend flowing in complex flow fields. A dilute emulsion of poly-dimethylsiloxane droplets immersed in a poly-isobutene matrix, both Newtonian liquids at room temperature, has been chosen as a model system. Optical microscopy coupled with image acquisition analysis allowed to monitor the behavior of droplets flowing through a sudden contraction and through a gradual converging channel followed by a sudden expansion. The experimental results indicate that drop deformation and breakup are sensitive to both shear and extensional components. A simple criterion, based on the evaluation of a local critical capillary number, is proposed to predict the morphological evolution of the flowing blend. By using computer simulations to estimate the velocity gradients in the flow field, it is shown that the proposed criterion is able to successfully predict the observed morphology. © 2001 Elsevier Science Ltd. All rights reserved.

Keywords: Polymer blends; Complex flow; Drop breakup

1. Introduction

The microstructure, or morphology, of immiscible polymer blends is a crucial factor in determining the material behavior in the processing stages as well as in the final use. Depending on the flow field applied in the processing apparatus, the blend morphology can be refined (due to drop breakup) or coarsened (due to coalescence events) [1,2]. A review of the mechanisms at the basis of the flow-induced morphology evolution can be found in Refs. [3,4].

Starting from the pioneering work of Taylor [5] optical microscopy techniques have been used to observe the morphology evolution of liquid emulsions during flow. Many studies have focused on the analysis of single drop deformation and breakup [4], whereas less work has been done in the field of drop coalescence [6–8]. Most of these studies have considered simple shear or simple extension flow conditions. In most processing applications, however, a complex flow field is encountered where shear and extensional components are present at the same time. Complex flow fields are important also when rheological measurements have to be interpreted. Han et al. [9], for example, suggested that the difference between capillary and cone and plate measurements of immiscible polymer blends is due to the morphological changes taking place in the entrance region, where a complex flow sets in.

Only few studies in the literature deal with morphology observations in complex flow conditions, particularly in the case of entry flows. Han and Funatsu [10] studied the deformation of single droplets in the complex flow developing in a sudden contraction. They found that the extensional flow field led to drop deformation in the entry section, but fibril breakup by Rayleigh instability set in only after entering the contraction. They also found that viscoelastic droplets were more stable than Newtonian ones. Similar results were reached by Chin and Han [11,12] who used a gradually converging channel geometry. The same geometry was used by Van Der Reijden-Stolk and Sara [13] to study the behavior of Newtonian droplets suspended in a Newtonian medium. By using an approximated analysis to derive the flow field kinematics, they showed that the theory of Cox [14] was able to predict relatively well the observed drop deformation. One main limitation of the above studies is that the drop size was comparable to the transverse dimension of the flow field. In these conditions, it is expected that the presence of the drop strongly alter the (already complex) flow field.

In this paper, the behavior of a model polymer blend in two complex flow geometries is observed in real time by optical microscopy. Moderately concentrated blends are

---

* Corresponding author. Tel: +39-081-768-2285; fax: +39-081-239-1800.

E-mail address: grizzuti@unina.it (N. Grizzuti).

PII: S0032-3861(01)00078-7

used, so that a relatively large drop population can be observed, thus obtaining quantitative information on average deformation and breakup as determined by the complex flow field. Furthermore, since drop size is relatively small compared to the flow geometry, the effect of the local velocity gradient field can be evaluated. With the aid of computer simulations of the flow field kinematics, a comparison between the experimental results in complex flows and theories for irreversible drop deformation in simple shear and extensional flow is presented.

2. Materials and methods

2.1. Experimental apparatus

A schematic view of the experimental apparatus is presented in Fig. 1. The core of the setup is the flow cell, a transparent, shallow slit die whose geometrical details will be described later. The flow is observed by means of an optical microscopy tube placed on one side of the cell. Light is provided by a microscope lamp mounted on the opposite side. The whole optical train is fixed to a system of three precision positioning stages. One horizontal stage allows for fine focusing along the channel thickness. The second horizontal stage allows for microscope movements along the channel width. The third, vertical stage moves the microscope along the slit vertical axis, corresponding to flow direction. The microscope tube is equipped with an objective (Zeiss Achroplanar, 10 × magnification), and a high resolution B/W CCD camera (Pulnix TMC76S), determining an image about 800 μm wide and 600 μm high. Images are video recorded on tape (Panasonic VHS professional recorder, mod. AG-7355), and subsequently digitized by a frame grabber (Data Translation, mod. DT-2867LC). An image analysis software (Global Lab Image) is used to process the image and obtain quantitative information on the flowing blend.

An exploded view of the flow cell is presented in Fig. 2(a). The cell is made up of two polycarbonate, transparent plates, separated by a metallic spacer. The shape of the spacer defines the flow cell geometry. The plates are held together by a double metallic frame, the whole setup being tightened by screws. A syringe pump (Harvard Apparatus mod. 909) guarantees the liquid feed through two symmetric holes drilled into the transparent plates. A check of the accuracy of the flow rate imposed by the pump was performed by weighing the polymer at the cell outlet.

Figs. 2(b) and (c) show the geometrical details of the two cell geometries used in the present work. The first cell (Fig. 2(b)) is a straight channel with an abrupt contraction. The larger upstream channel has a width $W_1 = 30$ mm and a length (measured from the center of the feeding hole to the contraction section) $L_1 = 21$ mm; after the contraction, the channel width is $W_2 = 3$ mm and the length $L_2 = 75$ mm. The second flow cell (Fig. 2(b)) includes a gradual converging section, followed by an abrupt expansion to the initial channel width. In this case, the width and length of the upstream channel are $W_1 = 40$ mm and $L_1 = 15$ mm, respectively. The length of the converging part is $L_2 = 10$ mm, with a minimum width $W_2 = 6$ mm; finally, in the downstream section $W_3 = W_1 = 40$ mm and $L_3 = 60$ mm. Both flow cells are characterized by a channel thickness $2\delta = 1$ mm.

2.2. Blend composition and properties

The immiscible blend investigated in the present work is

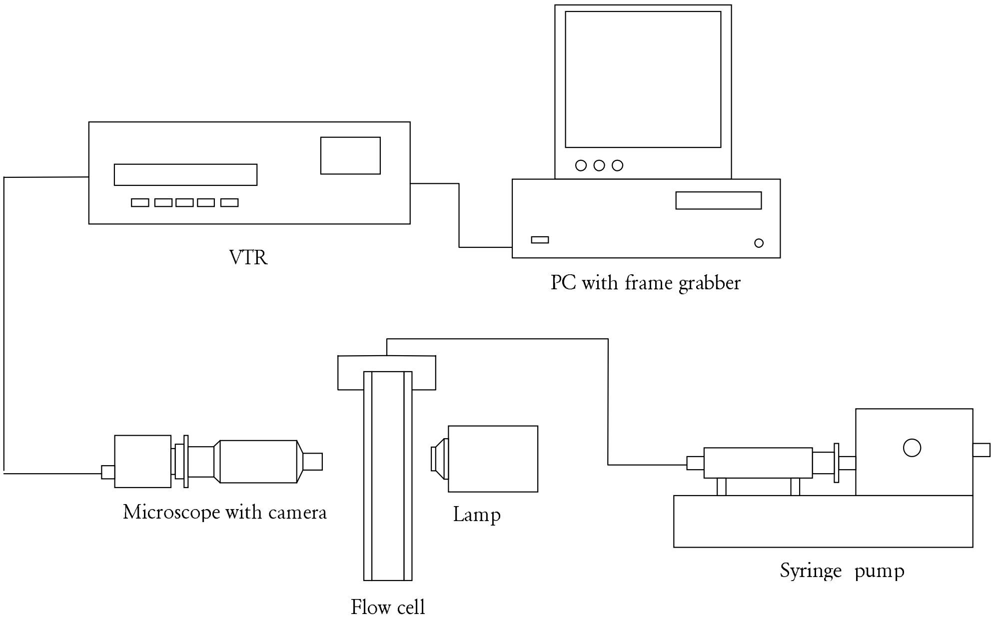

Fig. 1. Schematic view of the experimental setup.

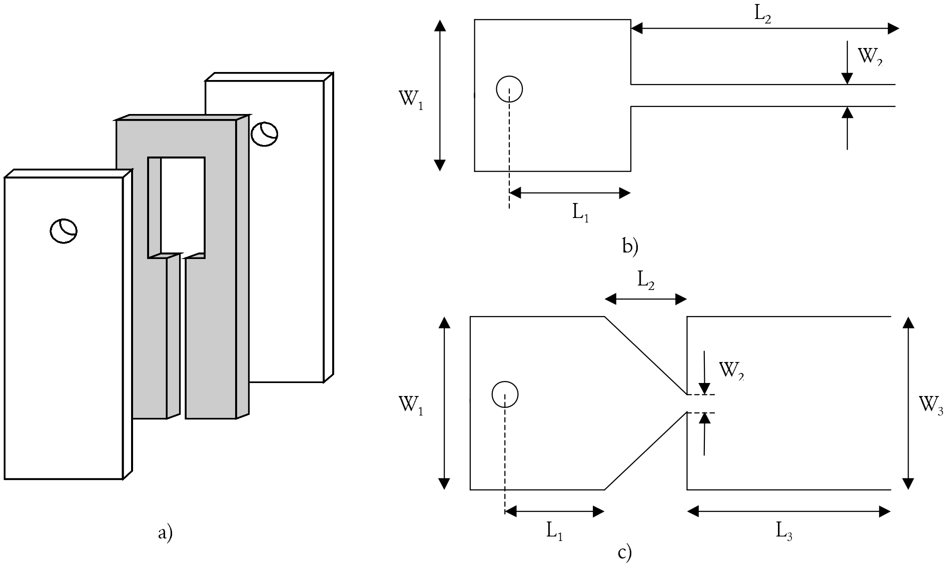

Fig. 2. (a) Schematic exploded view of the flow cell; (b) geometry of the abrupt contraction; (c) geometry of the gradual contraction followed by sudden expansion. See text for the meaning of symbols.

composed of poly-isobutene (PIB; Parapol 1300 from Exxon) and poly-dimethylsiloxane (PDMS; Rhodorsil 47V200.000 from Rhône-Poulenc). PIB and PDMS are transparent liquids at room temperature. Furthermore, the difference in their refractive index is large enough to guarantee good optical contrast. Although the blend is of no practical use, it represents a useful model system, which has been the subject of extensive investigations within the framework of an European Union research project [15]. The rheological and interfacial behavior of PIB and PDMS has been already studied elsewhere [16]. For the range of velocity gradients used in the present work, both liquids can be considered as Newtonian. A summary of their main physical properties is reported in Table 1.

PIB/PDMS blends were prepared by hand mixing suitable amounts of the two polymers. In order to remove the entrapped gas bubbles, blends were kept under vacuum overnight at room temperature. In this way, a homogeneous dispersion was obtained. Furthermore, a relatively narrow size distribution resulted with an average droplet size of about 15 μm, which is much smaller than the smallest flow field characteristic length ($2\delta = 1$ mm). By using this procedure, blends of PDMS in PIB with PDMS volume fraction of 0.5% were prepared. The concentration of the dispersed phase was chosen so as to obtain a system of non-interacting droplets, and to avoid superposition of droplets in the microscope field of view, thus allowing for an accurate measurement of their size and deformation. At the same time, the PDMS concentration was sufficient to produce a large population of drops, so that reliable averaged information could be extracted from the experimental runs. Only emulsions of PDMS droplets in PIB were prepared. The inverse blend was not used due to the non negligible solubility of PIB in PDMS, which results in PIB drop shrinkage especially at low concentrations of the dispersed phase [17].

Table 1
Physical properties of PIB and PDMS at 23°C

	Density (Kg/m^3)	Refractive index	Viscosity (Pa s)	Interfacial tension (N/m)
PIB	895	1.499	93	3×10^{-3}
PDMS	975	1.406	197	

2.3. Computer simulation

Finite element numerical simulations of the flow in the cell have been accomplished by means of the commercial software Polyflow® (release 3.3.0) implemented on a IBM-RISC6000-530 workstation. Due to the low concentration of PDMS in the blend, the flow was simulated by assuming Newtonian behavior with a viscosity equal to that of PIB. Since the maximum estimated Reynolds number for the flow is of the order of 10^{-4}, inertial terms have been neglected. A typical quadrilateral element grid was used, as well as quadratic and linear representation for the velocity and the pressure, respectively. The number of elements was chosen so as to guarantee a mesh-size independent solution.

3. Experimental results

Flow experiments were conducted with the two geometries described above and for different flow rates, as

Table 2
Summary of the flow experiments

	Flow rate (cm^3/s)		
Abrupt contraction	3.2×10^{-3}	5.7×10^{-3}	1.1×10^{-2}
Gradual contraction/abrupt expansion	1.6×10^{-3}	3.2×10^{-3}	5.7×10^{-3}

summarized in Table 2. It should be noted that the feeding syringe volume is of about 20 cm^3, to be compared with a flow cell volume of less than 4 cm^3. In a typical experiment, after the flow is set in, at least 8 cm^3 of fluid are pumped through the cell before measurements are started. This guarantees that (Lagrangian) steady-state conditions are reached into the cell. For each flow rate, the size and deformation of droplets flowing at the channel centerline were measured at different locations along the flow direction. A typical image used to determine drop size and deformation is presented in Fig. 3. A minimum of 50 droplets for each position was considered, and three runs were repeated for each flow rate. Good reproducibility was found between different runs at the same flow rates. The results presented below, therefore, report averages over the whole set of experiments.

3.1. Abrupt contraction

Figs. 4–6 report the results for the flow through the sudden contraction. In particular, the average major and minor axes of drops moving along the channel centerline are plotted as a function of the distance from the feeding gate. The two axes were always found to be parallel and perpendicular to the flow direction, respectively. The broken line marks the position of the contraction. The vertical bars at each data point (obtained as twice the distribution variance) represent the spread of the axis size distribution. It should be stressed that data points are the reflection of a large population of droplets (more than 150 drops for each point), and that plotted values are averages of measurements taken at varying depths across the channel thickness.

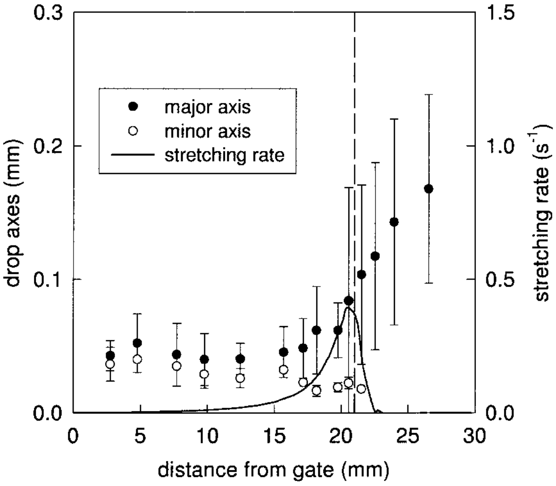

Fig. 4. Major and minor drop axes along the channel centerline for the abrupt contraction, as a function of the distance from the feeding gate, at the flow rate of 3.2×10^{-3} cm^3/s. The broken line marks the position of the contraction section. The solid line is the calculated average stretching rate profile along the channel centerline.

For all flow rates investigated, the general trend of the experimental results is the same. In particular, in the

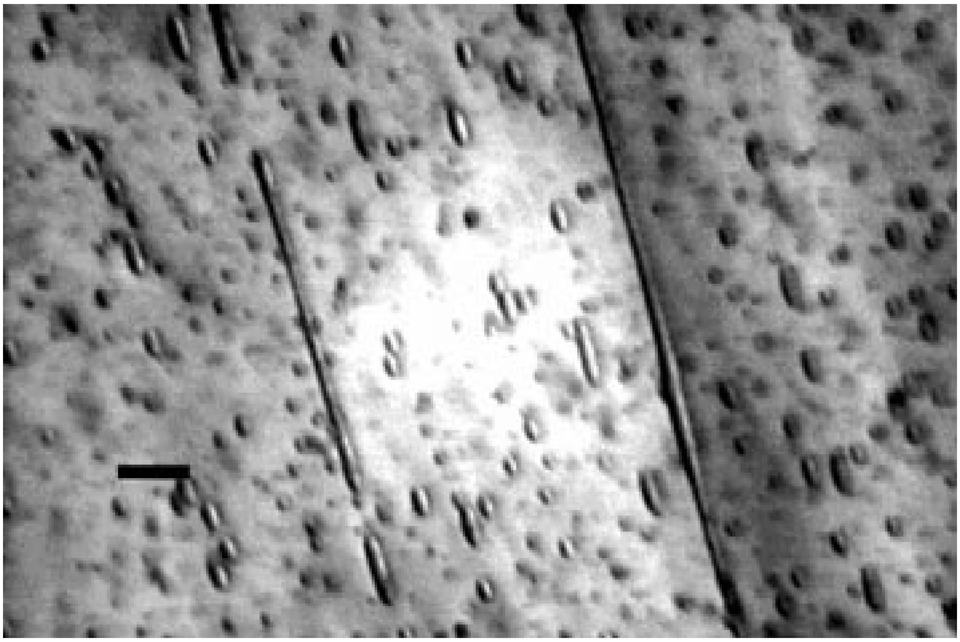

Fig. 3. Microscope image of the flowing blend. The image is taken about 3 mm before the abrupt contraction at a flow rate of 5.7×10^{-3} cm^3/s. The flow is from upper left to lower right. Deformed droplets as well as long filaments can be observed. The horizontal tick corresponds to a length of 100 μm.

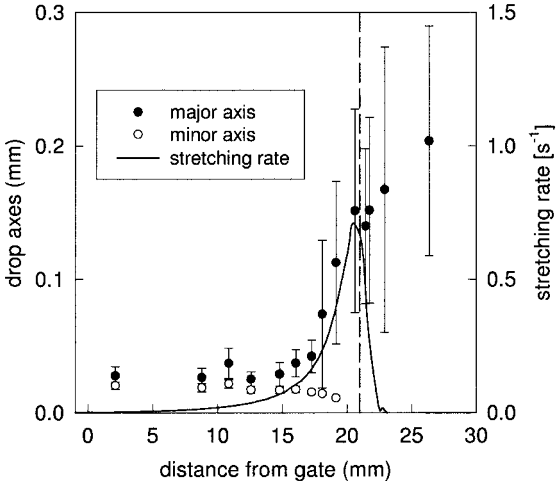

Fig. 5. Major and minor drop axes along the channel centerline for the abrupt contraction, as a function of the distance from the feeding gate, at the flow rate of 5.7×10^{-3} cm^3/s. Symbols and lines as in Fig. 4.

upstream region droplets are moderately elongated along the flow direction, as a result of the shear rate field acting along the thickness direction. As the converging section is approached, drop elongation increases. It must be noted that, when drop elongation becomes too high, quantitative measurements of the two axes become impossible: in fact, the minor axis becomes too small, its dimension falling below microscope resolution. Similarly, when the major axis becomes too long, only filaments of non-measurable length are observed.

Although the results for the three flow rates are similar, important differences are to be pointed out. At the lowest flow rate (3.2×10^{-3} cm^3/s, Fig. 4), drop elongation remains moderate in the contraction region. When droplets enter the narrower channel section, the deformation increases dramatically. As a result, drop width cannot be measured in this region. Likewise, major axis measurements in the downstream channel stop when all droplets are transformed into tiny, long filaments, which actually fill the whole microscope field of view. At the flow rate of 5.7×10^{-3} cm^3/s (Fig. 5), filaments develop well before the change of section. When entering the contraction, the elongated droplets essentially keep their degree of deformation. Finally, for the largest flow rate (1.1×10^{-2} cm^3/s, Fig. 6), the effect of the stretching flow is most apparent. Drops transform into long filaments well before the contraction section, and both their length and width soon become non measurable.

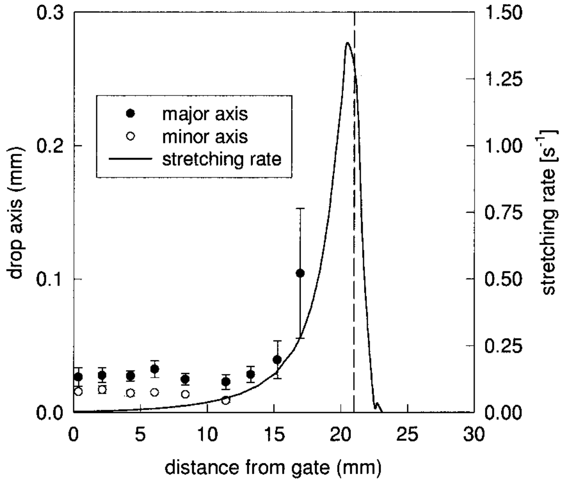

Fig. 6. Major and minor drop axes along the channel centerline for the abrupt contraction, as a function of the distance from the feeding gate, at the flow rate of 1.1×10^{-2} cm^3/s. Symbols and lines as in Fig. 4.

The morphology developed after the contraction was also observed along the downstream part of the slit. In all cases PDMS inclusions kept their filament shape for a long time after the contraction. In most cases, filaments eventually broke into very tiny droplets, whose size could not be measured because it was always below microscope resolution.

3.2. Gradual contraction followed by sudden expansion

Figs. 7–9 report the results for the second flow geometry, that is, a gradual converging channel followed by a sudden expansion. Here, the broken line marks the position of the expansion section, whereas the dotted line indicates the beginning of the converging region. For all flow rates considered, slightly elongated ellipsoids are observed in the upstream channel after the feeding gate. Drops become more elongated when approaching the converging section. Finally, after the expansion section, a less deformed configuration is recovered. Also in this type of flow, however, qualitative differences in the drop morphology are observed depending on flow intensity.

At the lowest flow rate (1.6×10^{-3} cm^3/s, Fig. 7), drops experience a reversible deformation. In fact, Fig. 7 shows that, after a relatively modest deformation in the converging section, drops recover an almost spherical shape after the expansion, with an average size, which is practically equal to the upstream value. Visual observation confirms the quantitative measurements, indicating that breakup is an infrequent event. Upon increasing the flow rate (3.2×10^{-3} cm^3/s, Fig. 8), a different morphology evolution is observed. In the contraction region drops are deformed into very elongated ellipsoids, which eventually breakup, mostly into two twin droplets, when flowing past the expansion. Fig. 8 clearly indicates the drop size reduction when moving from the upstream to the downstream section. Finally, at the highest flow rate (Fig. 9), strong drop deformation is generated in the converging section, such that filament width soon fall below microscope resolution and cannot be measured. Surprisingly, however, filaments are elongated even more after the expansion section, eventually breaking up only in the far downstream, well-developed flow region.

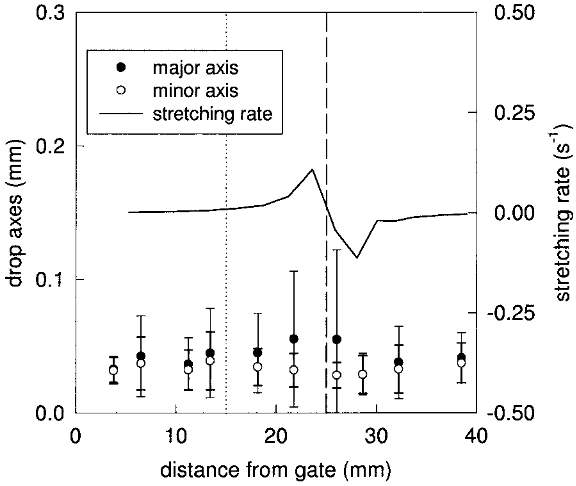

Fig. 7. Major and minor drop axes along the channel centerline for the gradual contraction followed by expansion, as a function of the distance from the feeding gate, at the flow rate of 1.6×10^{-3} cm^3/s. The broken line marks the position of the contraction section, the dotted line the beginning of the gradual contraction. The solid line is the calculated average stretching rate profile along the channel centerline.

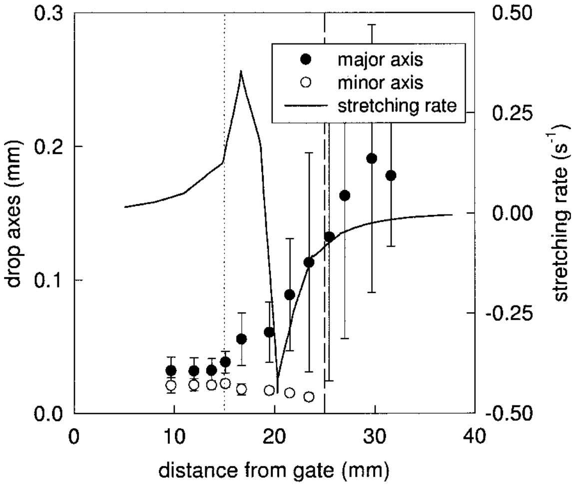

Fig. 9. Major and minor drop axes along the channel centerline for the gradual contraction followed by expansion, as a function of the distance from the feeding gate, at the flow rate of 5.7×10^{-3} cm^3/s. Symbols and lines as in Fig. 7.

4. Discussion

In Newtonian systems, drop deformation and breakup are controlled by two fundamental dimensionless parameters, i.e. the viscosity ratio

$$p = \frac{\eta_d}{\eta_m}, \tag{1}$$

where η_d and η_m are the droplet and matrix viscosity, respectively, and the capillary number

$$\mathrm{Ca} = \frac{\eta_m \kappa R}{\sigma}, \tag{2}$$

where κ is the characteristic velocity gradient ($\dot{\gamma}$ for shear flow and $\dot{\epsilon}$ for stretching flow), R the drop radius, and σ is the interfacial tension. The capillary number represents the ratio between flow and interfacial stresses. At a given p, drop deformation is an increasing function of Ca. When interfacial forces are no longer able to sustain the deformation induced by flow stresses, an irreversible deformation occurs, eventually leading to drop breakup. The onset of irreversible deformation is determined by a critical value of the capillary number, Ca_{cr}. Both theory and experiments [18–21] have confirmed that for a given type of flow Ca_{cr} is a unique function of the viscosity ratio. Furthermore, extensional flows are more effective than shear flow in generating drop breakup, as Ca_{cr} for extension is always lower than the corresponding shear value. For both shear and elongational flows, Ca_{cr} attains a shallow minimum for $0.1 \le p \le 2$. For shear flow, however, no Ca_{cr} can be found for $p > 4$, indicating that drops substantially more viscous than the matrix cannot be broken by a shear deformation.

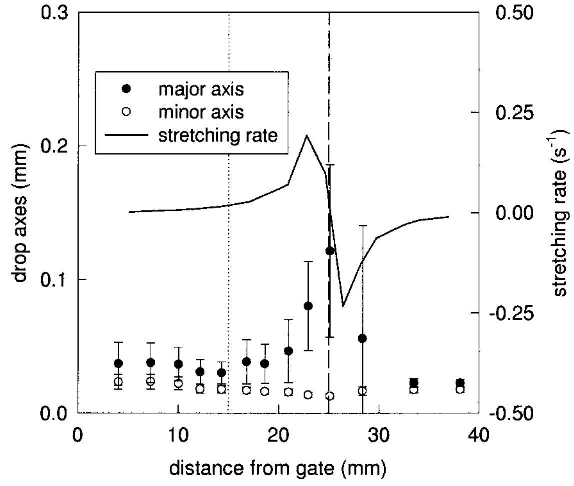

Fig. 8. Major and minor drop axes along the channel centerline for the gradual contraction followed by expansion, as a function of the distance from the feeding gate, at the flow rate of 3.2×10^{-3} cm^3/s. Symbols and lines as in Fig. 7.

The relations between Ca_{cr} and p just presented are valid only under the assumption of steady, homogeneous flow. For example, it has been shown that if the velocity gradient is increased in a sudden step, then the critical capillary number is reduced [19]. Obviously, steady homogeneous flow conditions do not hold for the experiments presented in the previous section. In fact, at least in the critical flow region, varying shear and extensional flow components coexist. However, a semi-quantitative interpretation of the experimental results can still be attempted if the following (crude) assumptions are made:

(i) at each position along the flow direction, shear and stretching rates averaged across the channel depth are considered;

(ii) the effects of shear and extensional components on droplet deformation are assumed to be mutually independent;

(iii) the state of deformation of the droplets depends only on the local level of shear and stretching rates, that is, pseudo-steady-state conditions are assumed for drop deformation.

Under the above assumptions, a simple criterion for drop breakup in complex flows can be envisaged. Droplets will be irreversibly deformed only when either the local stretching rate or the local shear rate exceed a critical value for breakup.

For shear flow, several empirical expressions for the critical capillary number as a function of the viscosity ratio have been proposed in the literature. In particular, experimental data are well fitted in the range $10^{-3} \leq p \leq 4$ by the following equation [21]:

$$\log \mathrm{Ca}_{\mathrm{cr}}^{\mathrm{sh}} = \log\left(\frac{\eta_{\mathrm{m}}\dot{\gamma}_{\mathrm{cr}}R_0}{\sigma}\right) = a + b\log p + c(\log p)^2 + \frac{d}{\log p - \log p_{\mathrm{c}}}, \tag{3}$$

where a, b, c, d, and p_{c} are known fitting parameters. Since the initial size of the droplets is $R_0 \cong 15$ μm, use of Eq. (3) with the physical constants reported in Table 1 gives

$$\dot{\gamma}_{\mathrm{cr}} = 1.54. \tag{4}$$

For extensional flows, expressions similar to Eq. (3) are not available for the viscosity ratio of the blend used in this work. Therefore, a critical capillary number has been extracted from the experimental data of Grace [20]

$$\mathrm{Ca}_{\mathrm{cr}}^{\mathrm{ext}} = \frac{\eta_{\mathrm{m}}\dot{\epsilon}_{\mathrm{cr}}R_0}{\sigma} \cong 0.27. \tag{5}$$

Eq. (5) yields the critical rate for extensional flow as

$$\dot{\epsilon}_{\mathrm{cr}} = 0.42. \tag{6}$$

4.1. Abrupt contraction

The local stretching and shear rates in the abrupt contraction flow have been computed by numerical simulation of the flow field. Since the upstream section of the channel is relatively long, a fully developed velocity profile has been assumed immediately after the feeding gate. The whole stretching rate profile along the channel centerline, that is, at the same position where experimental measurements were taken, is reported as a solid line in Figs. 4–6. As expected, $\dot{\epsilon}$ increases when moving towards the contraction, reaches a maximum just before it, then suddenly drops in the downstream part of the channel. Table 3 summarizes, for each flow rate, the essential information obtained from the simulation, that is, the shear rate in the wide upstream channel, $\dot{\gamma}_{\mathrm{up}}$, the maximum stretching rate in the contraction region, $\dot{\epsilon}_{\mathrm{max}}$, and the shear rate in the narrow downstream channel, $\dot{\gamma}_{\mathrm{do}}$. As said before, these values are averages over the channel thickness, and are computed at the channel centerline. Notice that $\dot{\gamma}_{\mathrm{do}}$ is more than ten times larger than $\dot{\gamma}_{\mathrm{up}}$, due to the 10:1 contraction ratio and the non-negligible effect of the channel finite width in the downstream section.

Table 3
The significant velocity gradients along the channel centerline for the abrupt contraction

Q (cm^3/s)	$\dot{\gamma}_{\mathrm{up}}$ (s^{-1})	$\dot{\epsilon}_{\mathrm{max}}$ (s^{-1})	$\dot{\gamma}_{\mathrm{do}}$ (s^{-1})
3.2×10^{-3}	0.32	0.40	4.6
5.7×10^{-3}	0.57	0.71	8.3
1.1×10^{-2}	1.12	1.4	16.2

Table 3 can be used to interpret the experimental results for the abrupt contraction. For all shear rates investigated, it is always verified that $\dot{\gamma}_{\mathrm{up}} < \dot{\gamma}_{\mathrm{cr}}$. This confirms the common feature of Figs. 4–6, since droplets flowing in the upstream section of the channel are subjected to a relatively small deformation to slightly elongated ellipsoids. For the lowest flow rate (Fig. 4), the stretching rate experienced by the droplets before the contraction lies below the critical value. As a consequence, also in this region drop deformation remains bounded. On the contrary, since $\dot{\gamma}_{\mathrm{do}} > \dot{\gamma}_{\mathrm{cr}}$, irreversible deformation is observed in the downstream channel. At the flow rate of 5.7×10^{-3} cm^3/s (Fig. 5), the maximum stretching rate overcomes the critical value for breakup. Droplets flowing towards the contraction along the centerline are gradually deformed above the irreversible threshold, and long filaments form. Since $\dot{\gamma}_{\mathrm{do}} > \dot{\gamma}_{\mathrm{cr}}$, filaments remain stretched in the downstream section as the shear flow ‘sustains’ the deformation and delays breakup by Rayleigh instability [22]. Finally, at the highest flow rate $\dot{\epsilon} > \dot{\epsilon}_{\mathrm{cr}}$ well before the contraction section. For this reason, as shown in Fig. 6, drops soon transform into very elongated and thin filaments.

4.2. Gradual contraction followed by sudden expansion

The flow field in this geometry, even along the channel centerline, is more complex than that developing in the sudden contraction, and can be qualitatively described as follows. The upstream section is characterized by a pure shear flow across the channel thickness. As the fluid enters the converging section extensional flow sets in. As shown by the solid lines in Figs. 7–9, the stretching rate reaches a maximum and then decreases towards the expansion section. The region immediately after the expansion is characterized by compression, radial flow. The stretching rate, therefore, becomes negative, attains a minimum, and gradually tends to zero. This happens in the far downstream section of the channel, where the pure shear flow is again recovered. Following the same trajectory, the shear rate gradually increases in the converging section, due to the increase in velocity related to the reduction of cross

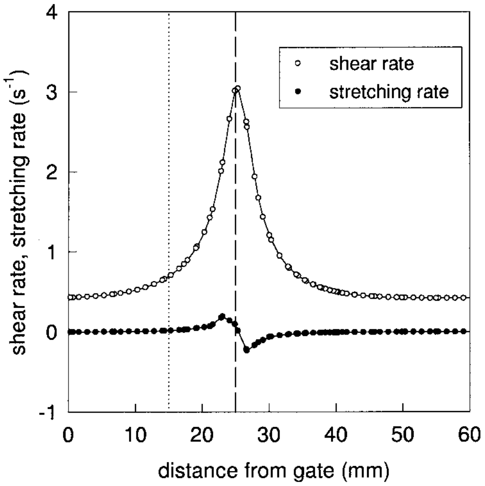

Fig. 10. Average shear rate and stretching rate profiles along the channel centerline for the gradual contraction followed by expansion at the flow rate of 3.2×10^{-3} cm^3/s.

sectional area. The shear rate reaches its maximum value at the expansion section. Here, due to the rearrangement of the velocity profile across the channel width, the shear rate at the centerline decreases only gradually towards its final value. The shear rate profile at the centerline for the flow rate of 3.2×10^{-3} cm^3/s, as computed by the Polyflow simulation, is reported in Fig. 10. The stretching rate profile, already shown in Fig. 8, is also reported for comparison. Notice that, since the upstream and the downstream cross sections are the same, the initial and final shear rates are equal.

Table 4 summarizes the relevant results of the flow simulation for this geometry at the flow rates used in the experiments. $\dot{\gamma}_{\mathrm{up}} = \dot{\gamma}_{\mathrm{do}}$ is the shear rate in the far upstream and far downstream regions of the channel, $\dot{\epsilon}_{\max}$ the maximum stretching rate attained in the converging region, and $\dot{\gamma}_{\max}$the maximum shear rate at the expansion section. Like Table 3, values are averages over the channel thickness, and are computed at the channel centerline.

Comparison of Table 4 with the experimental results of Figs. 7–9 suggests the following interpretation. For all flow rates investigated, the far upstream and far downstream shear rates and the stretching rate are below the corresponding critical limits for droplet breakup. Therefore, the major role is played by the shear rate profile in the proximity of the sudden expansion. In fact, for the lowest flow rate, one has $\dot{\gamma}_{\max} < \dot{\gamma}_{\mathrm{cr}}$, that is, droplets flowing along the centerline cannot be broken up by the flow. This confirms the experimental results of Fig. 7, where only slight deformation and no breakup are observed. Upon increasing the flow rate the condition $\dot{\gamma}_{\max} > \dot{\gamma}_{\mathrm{cr}}$ is reached, and a shear rate larger than the critical value is attained both before and after the expansion section. As a consequence, drops are deformed irreversibly. After the expansion, the combined action of compression and shear flow leads to a simultaneous relative contraction and twin-type breakup of the drops, as confirmed by Fig. 8. Finally, for the highest shear rate, shear flow is definitely the dominant factor in determining the drop morphology. In this case, $\dot{\gamma}_{\max} \gg \dot{\gamma}_{\mathrm{cr}}$, whereas $\dot{\epsilon}_{\max}$ is still well below the critical value for breakup. Drops deform into long filaments, with deformation still taking place long after the expansion section, and eventually leading to breakup into very small droplets by Rayleigh instability in the far downstream region of the channel (see Fig. 9).

Table 4
The significant velocity gradients along the channel centerline for the gradual contraction followed by sudden expansion

Q (cm^3/s)	$\dot{\gamma}_{\mathrm{up}} = \dot{\gamma}_{\mathrm{do}}$ (s^{-1})	$\dot{\epsilon}_{\max}$ (s^{-1})	$\dot{\gamma}_{\max}$ (s^{-1})
1.6×10^{-3}	0.20	0.095	1.5
3.2×10^{-3}	0.40	0.19	3.0
5.7×10^{-3}	0.71	0.33	5.3

5. Concluding remarks

The experimental results of this paper, coupled with a computational analysis of the flow field, clearly show that the morphology of a blend is strongly affected by the complex nature of the flow. The two geometries used, that is, a sudden contraction and a gradual converging channel followed by a sudden expansion, can be seen as useful model analogs of typical processing applications, such as those encountered in polymer injection molding. It has been shown that the flow-induced morphological evolution can be predicted (at least semi-quantitatively) by assuming that the extensional and shear flow components act independently in determining the deformation and the possible breakup of the dispersed phase. The general criterion, which has proven successful at least for the system studied here, is that droplet breakup takes place when either the local shear rate or the local stretching rate, which can be determined by computer simulation, exceed the critical value for breakup as obtained from steady homogeneous flow data.

This work does not have the presumption to be at all conclusive. More experimental data on different blend systems and flow geometries are needed, in order to validate the conclusions reached here. It must be also stressed that some important factors affecting the morphological evolution of polymer blends in complex flows have been deliberately ignored. For example, the choice of a very dilute dispersion, though necessary for experimental needs, implies that coalescence phenomena have not been taken into account. It is well known, conversely, that coalescence can play a major role in determining the flow induced morphology in real, concentrated polymer blends [2]. Furthermore, the use of a Newtonian (though highly viscous) model blend constitutes another, obvious limitation, as the role of viscoelasticity on the morphology evolution even in homogeneous flows is nowadays not at all understood.

Acknowledgements

The financial support of European Union (contract BRE2CT920213), and of Consiglio Nazionale delle Ricerche (contract 97.02821.CT03) is gratefully acknowledged.

References

[1] Utracki LA, Shi ZH. Polym Engng Sci 1992;32:1824–33, 1834–45, 1846–56.
[2] Sundararaj U, Macosko CW. Macromolecules 1995;28:2647–57.
[3] Han CD. Multiphase flow in polymer processing. New York: Academic Press, 1981. Chap. 5.
[4] Elmendorp JJ. Dispersive mixing in liquid systems. In: Rauwendaal C, editor. Mixing in polymer processing. New York: Marcel Dekker, 1991. p. 17–100.
[5] Taylor GI. Proc R Soc Lond 1934;A146:501–23.
[6] Grizzuti N, Bifulco O. Rheol Acta 1997;36:406–15.
[7] Vinckier I, Moldenaers P, Terracciano AM, Grizzuti N. AIChE J 1998;44:951–8.
[8] Al-Mulla A, Gupta RK. Rheol Acta 2000;39:20–5.
[9] Han JH, Choi.-Feng C, Li D-J, Han CD. Polymer 1995;36:2451–62.
[10] Han CD, Funatsu K. J Rheol 1978;22:113–33.
[11] Chin HB, Han CD. J Rheol 1979;23:557–90.
[12] Chin HB, Han CD. J Rheol 1980;24:1–37.
[13] Van Der Reijden-Stolk C, Sàra A. Polym Engng Sci 1986;26:1229–39.
[14] Cox RG. J Fluid Mech 1969;37:601–23.
[15] BRITE/EURAM Project, Contract BRE-CT92-0213. Intelligent processing for customised polymer blends, Final Technical Report, 1997.
[16] Sigillo I, di Santo L, Guido S, Grizzuti N. Polym Engng Sci 1997;37:1540–9.
[17] Guido S, Simeone M. J Fluid Mech 1998;357:1–20.
[18] Rallison JM. Annu Rev Fluid Mech 1984;16:45.
[19] Bentley BJ, Leal LG. J Fluid Mech 1986;167:241–83.
[20] Grace HP. Chem Engng Commun 1982;14:225–77.
[21] De Bruijn RA. PhD Thesis, Eindhoven University of Thechnology, Eindhoven, The Netherlands, 1989.
[22] Khakhar DV, Ottino JM. J Fluid Mech 1986;166:265–85.